# Reactivity Determinants in Electrodeposited Cu Foams for Electrochemical $CO_2$ Reduction

Katharina Klingan[a]#, Tintula Kottakkat[b]#, Zarko P. Jovanov[c], Shan Jiang[a], Chiara Pasquini[a], Fabian Scholten[d], Paul Kubella[a], Arno Bergmann[c,e], Beatriz Roldan Cuenya[d,e], Christina Roth*[b], Holger Dau*[a]



**Abstract:** Electrochemical $CO_2$ reduction is of high interest for production of non-fossil fuels. The reactivity of eight Cu foams with substantial morphology differences was comprehensively investigated by analysis of product spectrum and electrochemical *in-situ* spectroscopies (XANES, EXAFS, XPS, Raman). This approach provided new insight in reactivity determinants: (1) Morphological details, (2) stable Cu oxide phases, and (3) *CO poisoning of $H_2$-formation are not decisive. (4) The electrochemically active surface area (ECSA) determines reactivity trends. (5) Macroscopic diffusion limits the proton supply, resulting in pronounced alkalization at CuCat surfaces (*operando* Raman spectroscopy). We propose: (6) $H_2$ and $CH_4$ formation are suppressed by macroscopic buffer alkalization, whereas CO and $C_2H_4$ formation still proceed via a largely pH-independent mechanism. (7) $C_2H_4$ is formed from two CO precursor species, namely adsorbed *CO and dissolved CO present in the foam cavities.

## Introduction

Selective conversion of $CO_2$ into high quality chemical feedstock and fuels represents an emerging energy storage technology.[1] The electrochemical reduction of carbon dioxide is a promising way of utilizing intermittently available renewable energies to produce chemical feedstock and fuels for later use. Presently, copper is in focus because of its ability to catalyze the electrochemical reduction of $CO_2$ into energy-dense hydrocarbons.[2] However, the electrochemical reduction of $CO_2$ on copper results in many different compounds formed at a wide range of overpotentials. In addition to undesired $H_2$, CO and mainly C1 and C2 hydrocarbons as wells as alcohols are formed in the gas headspace and in the liquid electrolyte. In recent years, there has been increasing effort to establish the control over product distribution by fine tuning of the physical properties of the Cu electrode.[3] So far, different strategies have been proposed for improving the activity and selectivity[4], among them are the variation in thickness of Cu metal over-layers[5], adjustment of size[6], shape[7], interparticle distance of nanoparticles[6b], selection of single crystal facets[6c, 8], the utilization of electrolyte properties[9], and grain boundary strain effects[10].

The influence of the roughness or specific nanostructures of the Cu electrode surface likely is of high importance.[11] Cu electrodes with high surface areas mainly produce C2 products such as $C_2H_4$ and $C_2H_6$.[3b, 12] However, high surface area gas diffusion electrodes favor the C1 pathway.[13] The CO yield at low potentials may or may not relate to the $C_2H_4$ yield at higher potentials.[6c, 7c, 11, 14] In any event, adsorbed CO, denoted as *CO, is a crucial reaction intermediate in production of CO, $CH_4$, and $C_2H_4$.[15] Increasing the relative amount of *CO sites favors elevated $C_2H_4$ activity.[10d, 14c, 16] *CO intermediates may be favored by local alkalization and mass transport limitations of protons.[9d, 17] Local pH changes probably lead to a change in reaction kinetics as the $CO_3^{2-}/HCO_3^-$ equilibrium is shifted, and $CO_2$ may be depleted from the electrode surface.[17b, 18] The influence of surface area and roughness on the product spectrum may relate to the strength of local alkalization.[17b, 19]

Incorporation of $Cu_2O$ into the bulk or the surface of the Cu electrodes may enhance the selectivity towards $C_2H_4$ and $C_2H_6$ strongly[3b, 7c, 11]. Ex-situ XRD measurements resulted in contradicting conclusions regarding the presence and stability of $Cu_2O$ species in Cu foams: (i) no $Cu_2O$[20], (ii) the presence of $Cu_2O$ after deposition[21], (iii) $Cu_2O$ reduction to $Cu^0$ during operation at catalytic potentials[21b], (iv) and the presence of $Cu_2O$ after operation at reductive potentials[22]. Huan et al. quantified a 10 % $Cu_2O$ mass contribution in their foams and 5 % of this phase was unaffected by cathodic electroreduction.[22a] *In-situ* deposition of a related dendritic Cu/$Cu_2O$ catalyst showed a stable cuprite phase after electrolysis at negative potentials in the regime of ethylene formation.[22b] Oxygen species may be merely products of air exposure, as recently shown for oxide-derived Cu catalysts,[23] so that reduction of copper oxide species precedes onset of $CO_2$ reduction.[24]

To shine light on the role of oxide species, we studied Cu foams by *operando* X-ray spectroscopy (XAS) and *quasi in-situ* X-ray photoelectron spectroscopy (XPS). The porous Cu films (called CuCats in the following) were electrodeposited using the dynamic hydrogen-bubble template method[21a]. For the first time, local pH

# these authors contributed equally to this work
[a] Dr. Katharina Klingan, Shan Jiang, Chiara Pasquini, Paul Kubella, Prof. Dr. Holger Dau
Department of Physics, Freie Universität Berlin
Arnimallee 14, 14195 Berlin
E-mail: holger.dau@fu-berlin.de
[b] Dr. Tintula Kottakkat, Prof. Dr. Christina Roth
Department of Chemistry, Freie Universität Berlin
Takustr. 3, 14195 Berlin
[c] Dr. Zarko Jovanov, Dr. Arno Bergmann
Department of Chemistry, Technische Universität Berlin
Straße des 17. Juni, 10623 Berlin
[d] Fabian Scholten,
Department of Physics, Ruhr University Bochum
Universitätstraße 150, 44801 Bochum
[e] Prof. Dr. Beatriz Roldan Cuenya
Fritz Haber Institute of the Max Planck Society
Faradayweg 4-6, 14195 Berlin

values at the Cu cathode during $CO_2$ electroreduction were experimentally addressed via *operando* Raman spectroscopy, based on analysis of the shift in the $HCO_3^-/CO_3^{2-}$ equilibrium. For eight foams with substantial morphology differences, we show how the area ratio of inner-foam surface ($A_{int}$) and macroscopic, outer surface ($A_{out}$) determines the partial current densities for formation of $H_2$, $CH_4$, CO, and $C_2H_4$ in distinctively different ways.

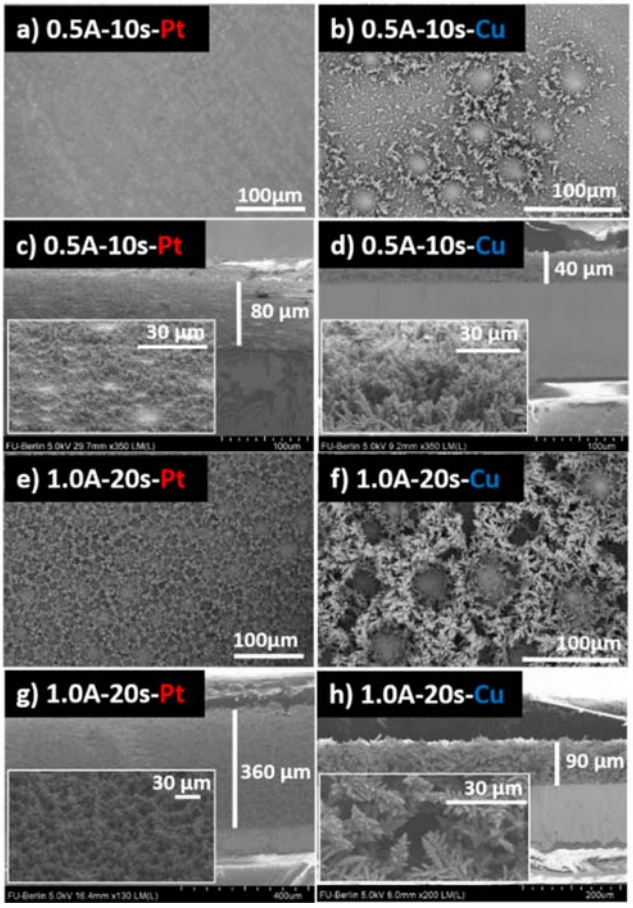


**Figure 1**. SEM of CuCats. Top-view of CuCats electrodeposited at (a) 0.5 A $cm^{-2}$ for 10 s on Pt, (b) at 0.5 A $cm^{-2}$ for 10 s on Cu, (e) at 1.0 A $cm^{-2}$ for 20 s on Pt, and (f) at 1.0 A $cm^{-2}$ for 20 s on Cu. Cross-sections of CuCats electrodeposited at (c) 0.5 A $cm^{-2}$ for 10 s on Pt, (d) at 0.5 A $cm^{-2}$ for 10 s on Cu, (g) at 1.0 A $cm^{-2}$ for 20 s on Pt, and (h) at 1.0 A $cm^{-2}$ for 20 s on Cu. Under the catalyst layer the metal substrate and silicon glue are visible, above copper tape, which was used to fix the sample on the sample holder. The insets show a magnified region of the cross section. Complete cross-sections of all investigated CuCats are shown in Figure S1, complete SEM topographies in Figures S2, S3.

## Results and Discussion

### Relevant physical properties – foam thickness, density, morphology and electrochemically active surface area

Material properties of the CuCats can be tuned by the electrodeposition process. Films of different thickness (Figure S1) with different micro-morphological structure (Figures S2, S3) were realized by variation of deposition current, time of deposition and substrates (Cu or Pt). Figure 1 shows the top-view and the cross-sectional scanning electron micrographs (SEM) of selected CuCats electrodeposited on Pt or Cu substrate either at low current densities, short time (0.5 A $cm^{-2}$ and 10 s), or at doubled current and time (1.0 A $cm^{-2}$ and 20 s). The thickness of the catalyst film on Pt is significantly higher (80-360 µm) than on Cu (40-90 µm). The influence of the substrate is reflected in pronounced differences in morphology of the CuCats on Pt metal (Figure S2) and Cu metal (Figure S3). Aside from internal porosity and dendritic structures, there are vertical macropores limited by dendritic structures (with pore diameters around 35 µm), which form a network of craters on the catalyst surface (Figure 1f). The pronouncedly different morphologies relate to the specific parameters of the here used 'bubble-template' approach.[25] Surface pore sizes increase with deposition time and higher deposition current; larger pores and more pronounced fractal structures are created on Cu metal. Pore formation depends on a complex process involving nucleation, growth, and detachment of $H_2$ gas bubbles during Cu electrodeposition.[25] Small $H_2$ bubbles are released fast on Pt, while on Cu $H_2$ desorption is slower, resulting in larger pores and deposition of less material.

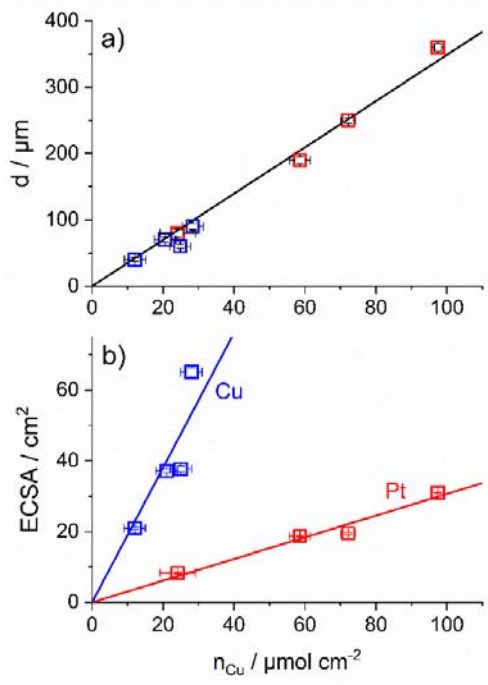


**Figure 2.** (a) Relation between the thickness (*d* in µm), of the CuCat films and the electrodeposited amount of metal ions ($n_{Cu}$ in µmol per geometrical surface area in cm²). (b) Relation between the electrochemically active surface area (ECSA in cm²) of various CuCat films and the electrodeposited amount of metal ions ($n_{Cu}$ in µmol per geometrical surface area in cm²). CuCats electrodeposited on Cu substrate are shown in blue, and on Pt substrate in red. The thickness of the samples was estimated from SEM cross-sections (Figure S1). The amount of deposited Cu material was determined from TXRF elemental analysis (Figure S4). The ECSA was calculated as $ECSA=C_{DL}/C_{Cu\ metal}$. The double layer capacitance ($C_{DL}$) was determined from scanning multiple CVs at different scan rates in a non-Faradaic current range (Figures S6, S7).

A linear relation between Cu amount and film thickness (Figures 2, S4, S5) indicates that the overall Cu density of the investigated porous CuCats is approximately the same ($\rho$=0.20±0.03 g $cm^{-3}$ versus 8.94 g $cm^{-3}$ for pore-free metallic Cu metal foil). We thus conclude that the CuCats are low-density foams (~45 times lower than Cu metal). Surprisingly, macroscopic foam density is roughly constant, regardless of the pronounced morphology differences at the nanometer and micrometer scale.

ECSAs were determined by cyclic voltammetry (CV) measurements at different scan rates in the non-Faradaic current region (Table S1, Figures S6, S7). For both substrate materials, the ECSA depends, to a first approximation, linearly on the electrodeposited Cu amount, but the electrochemical surface area per deposited Cu atom is 6 times higher for the films deposited on a Cu foil (1.90 cm² µmol$^{-1}$ for Cu substrate, 0.31 cm² µmol$^{-1}$ for Pt substrate). This difference is in qualitative agreement with the SEM results shown in Figure 1, which also suggest a clearly larger surface area for CuCat deposition on a Cu foil.

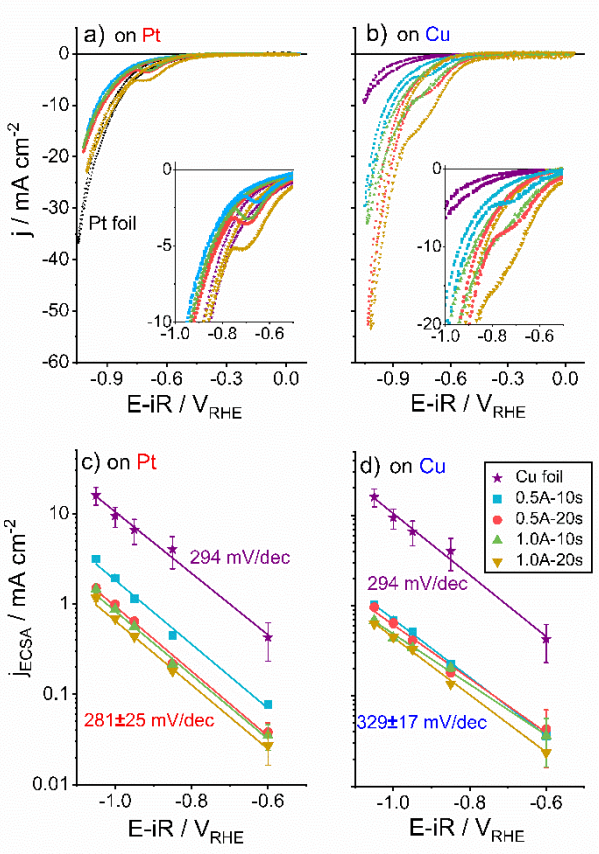


**Figure 3.** (a, b) CVs in 0.1 M $CO_2$ saturated $KHCO_3$ (pH=6.8, $CO_2$ flow rate=20 ml min$^{-1}$, scan rate =100 mV s$^{-1}$): CuCats deposited at 0.5 A cm$^{-2}$ for 10 s (cyan), at 0.5 A cm$^{-2}$ for 20 s (red), at 1.0 A cm$^{-2}$ for 10 s (green), at 1.0 A cm$^{-2}$ for 20 s (brown), Pt foil (black), and Cu foil (violet), on Pt substrate (a) or Cu substrate (b). The insets show the enlarged region of reduction waves originating most likely from *CO adsorption. (c, d) ECSA normalized current density during 1 h of chronoamperometric measurements as a function of applied potential vs. RHE for Cu foil (violet), and for CuCats deposited on Pt (c) and Cu substrate (d) at 0.5 A cm$^{-2}$ for 10 s (cyan), at 0.5 A cm$^{-2}$ for 20 s (red), at 1.0 A cm$^{-2}$ for 10 s (green), at 1.0 A cm$^{-2}$ for 20 s (brown). Tafel slope for Cu foil (violet) and averaged Tafel slopes with the corresponding standard deviations for CuCats/Pt – red and CuCats/Cu – blue.

### Total current densities and *CO current wave

*Total current density*. The electrochemical characterization of the catalysts was carried out in 0.1 M $KHCO_3$ solution saturated with $CO_2$ at a pH of 6.8 in a custom-built H-cell (Figure S9). To ensure that initially present, but unstable Cu oxide phases get reduced to metallic Cu (see 1$^{st}$ cycle of CV in Figure S10), we swept the potential between 0 and -1.2 $V_{RHE}$ with high scan rates (100 mV/s) until reproducible currents were obtained (CVs in Figure 3), then performed slow linear sweep voltammetry (5 mV/s, Figure S11). Highly similar qualitative characteristics are observed for LSV and CV: The onsets of cathodic currents are significantly shifted to more positive potentials for CuCats of varying deposition currents and times of synthesis compared to metallic Cu foil. The overpotential necessary to reach -5 mA cm$^{-2}$ is lowered up to 350 mV by CuCats in contrast to pure Cu. All CuCats reach significantly larger current densities (up to 5 times) than Cu metal foil. CuCats have ~8-65 times higher surface area than Cu metal foil (Figure 2), which most likely relates to the larger current densities. However, the ECSA-normalized current densities of the CuCats are by about one order of magnitude lower than for a pure Cu foil (Figure 3c and d). Surprisingly, the Tafel slope (Figure 3c and d) is similar for all catalyst materials (about 300 mV per decade). This unusually high value for the Tafel slope may reflect a diffusion limitation that is common to all investigated catalysts (even to the pure metal foil).

**CO current wave*. A current plateau is observed for all the CuCats around -0.57 $V_{RHE}$ in the LSVs (Figure S11, Figure S12) and from around -0.65 to -0.70 $V_{RHE}$ in the CVs (Figure 3a-b). This current wave has been attributed mostly to $CO_2$ reduction coupled to formation of adsorbed *CO,[14c, 15a, 26] but also to reduction of $HCO_3^-$ to $HCOO^-$.[27] Because the current-wave magnitude did not correlate with $j_{HCOO^-}$ (Figure S13), but is proportional to $j_{CO}$ (as shown later in Figure 8), we favor the assignment to adsorbed *CO. For a polycrystalline Cu metal foil with a low amount of defect sites[28], the *CO current wave has not been detectable. It also is invisible in the CVs we collected for the Cu metal foil, but clearly visible in all Cu foams (Figure 3a, 3b, S14; see Figure S15 for the corresponding redox charges obtained by integration of current waves). Extension of the potential window to more positive potentials did not affect the size of this current plateau (Figure S16a). However, when the CV scan was started at more negative potentials, the current plateau decreased (Figure S16b and c), suggesting that unbinding of *CO proceeds only at potentials more positive than about -0.4 $V_{RHE}$, in line with recent findings on CO desorption.[29] Variation of the scan rate suggests involvement of a diffusion limitation in *CO formation (Figure S17).

### Oxide content of Cu foams

To gain insight into the structure of the catalysts, *ex-situ* X-ray diffraction (XRD) patterns of different CuCats after a cycling protocol (three CVs and a LSV) were recorded (Figure S18). The

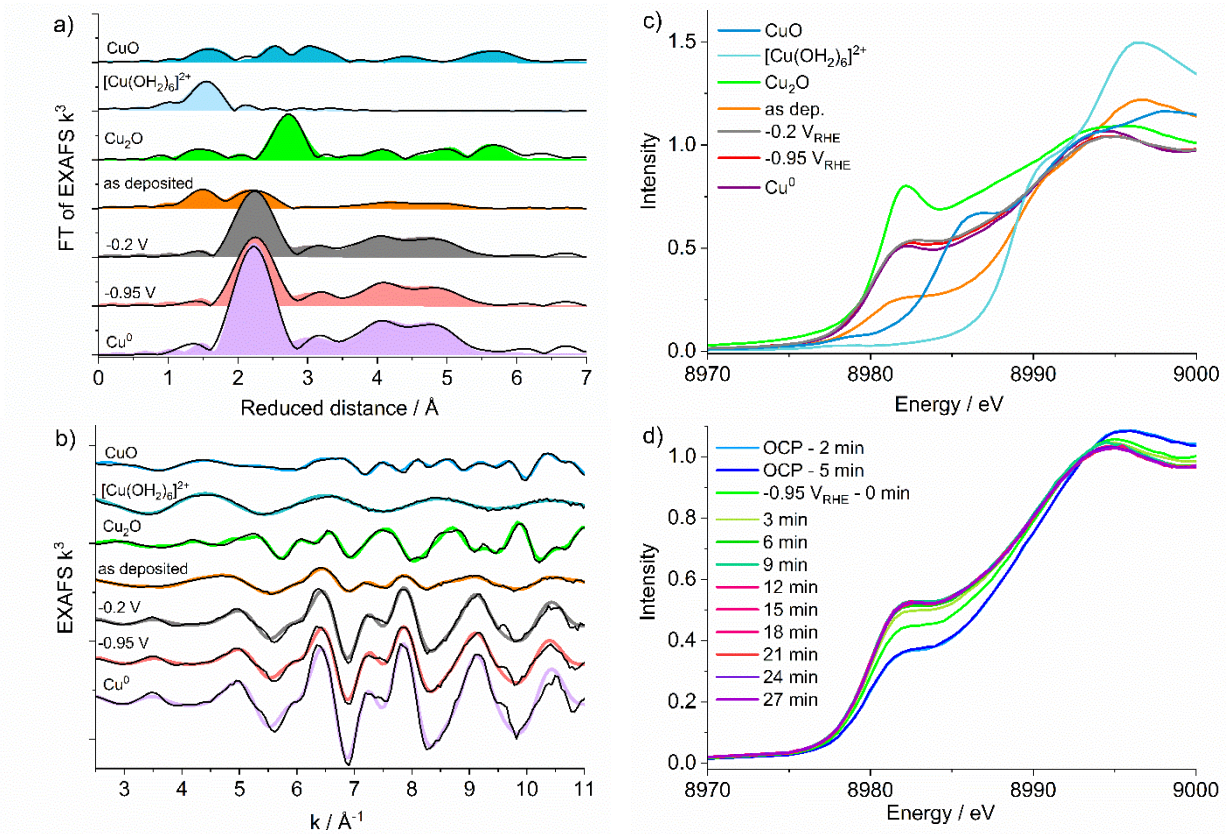


**Figure 4.** Analysis of the Cu oxide content by (*operando*) X-ray absorption spectroscopy at the Cu K-edge. a) Fourier-transformed $k^3$-weighted EXAFS spectra. Solid lines represent the experimental data and shading the EXAFS simulation. The indicated reduced distances are about 0.4 Å shorter than the real distance determined by EXAFS simulations (Table S2). b) $k^3$-weighted EXAFS spectra and simulations (colored lines) before Fourier transformation. c) XANES spectra at the Cu K-edge. Panels *a*, *b, c* contain data for $Cu^0$ (violet), CuCat at -0.95 $V_{RHE}$ (red), at -0.2 $V_{RHE}$ (grey), as deposited (orange), $Cu_2O$ (green), $[Cu(OH_2)_6]SO_4$ (light blue), the $Cu^{2+}$ ion in aqueous solution (blue). d) XANES at the Cu K-edge: CuCat in 0.1 M $KHCO_3$ (pH 6.8) at open circuit potential (OCP), and at -0.95 $V_{RHE}$ for the shown time values, which indicate when the XANES scan was started (each scan was collected within 3 min).

main phase of the catalysts was identified as metallic Cu with major contributions from crystallites of ~100 nm. A minor and separated phase was identified as $Cu^{I}_2O$ stemming from significantly smaller particles (<10 nm). $Cu^{II}O$ crystallites were not detected.

For further structural information—specifically on XRD-invisible, non-crystalline CuCat fractions—Cu *K*-edge X-ray absorption spectroscopy (XAS) was performed on dry (electrolyte-free) CuCat foams at 20 K (frozen after having performed a cycling protocol consisting of three CVs and one LSV). XANES (X-ray absorption near edge structure) spectra of the CuCats resemble a mixture of a Cu metal contribution and $Cu_2O$ contribution (Figure S20). Calculating linear combinations of $Cu^0$ metal foil and $Cu^{I}_2O$ (with the weighting factors as fit parameters) leads to identical results for XANES and EXAFS (extended X-ray absorption fine structure) spectra, namely the presence of 15% to 45% $Cu_2O$ (Figure S20).

The reason for the presence of the $Cu^{I}_2O$ detected by cryo-XAS on dried CuCat foams could be either (i) the presence of stable $Cu^{I}_2O$[30], or (ii) re-oxidation originating from air exposure[23] before freezing and execution of the cryo-XAS experiment. To address the role of air oxidation, we have selected a CuCat (Cu 0.5A-20s) to be studied by *operando* (or *in-situ*) XAS. In Figure 4a-c, the EXAFS and XANES of the films directly after electrodeposition, and at -0.2 and -0.95 $V_{RHE}$ (applied for 30 min each before collecting the data) are compared to reference substances (Cu metal, $Cu_2O$, CuO, and $[Cu(OH_2)_6]SO_4$). The as-deposited film contains Cu-O distances at 1.92 Å assignable to $Cu^{2+}$ (Table S2), and three Cu-Cu distances assignable to metallic Cu (2.51, 3.58, 4.41 Å). Applying a potential of either -0.2, or -0.95 $V_{RHE}$ for 30 min, the film gets reduced to a metallic copper of comparably low order, similar to observations reported for Cu nanocubes.[31] To assess how fast these reductive changes occur at the negative operating $CO_2$ reduction potential (-0.95 $V_{RHE}$), we have immersed the as-deposited CuCat into the $CO_2$-reduction buffer (0.1 M $KHCO_3$, pH 6.8) for various amounts of time (Figure 4d). Already under OCP (open-circuit potential) conditions, a major fraction of the Cu oxide becomes reduced. The XANES spectrum collected after 9 min at -0.95 $V_{RHE}$ indicates essentially complete reduction to metallic copper; no more further spectral changes are observed for the following 18 min at -0.95 $V_{RHE}$. Deconvolution of the final reduced state at -0.95 $V_{RHE}$ yielded a portion of 0-5% of $Cu_2O$ (Figure S21). This means that the complete absence of any $Cu_2O$ fraction is compatible with the spectra. Comparison with the spectrum collected at -0.2 $V_{RHE}$ reveals that already at low negative potentials (-0.2 $V_{RHE}$) the CuCat is in its most reduced state, which could be oxide-free state.

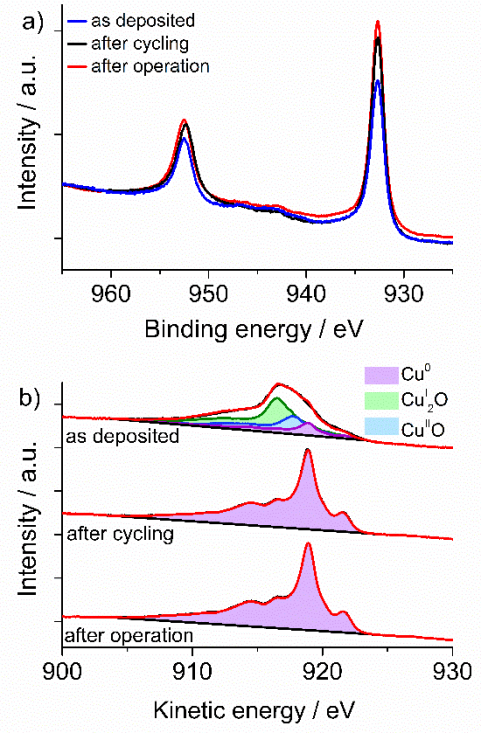


**Figure 5**. Quasi *in-situ* XPS measurements after ultra-high vacuum (UHV) transfer of CuCat deposited at 0.5 A $cm^{-2}$ for 20 s on Cu substrate, obtained directly after electrodeposition (as deposited), after performing three CVs and 1 LSV (after cycling - Figure S10; S11), and after 20 min of operation at -0.95 $V_{RHE}$ in 0.1 M $KHCO_3$, saturated with $CO_2$, pH 6.8. a) Binding energy of the Cu 2p region. b) Kinetic energy of the Cu LMM Auger region.

Additionally, the surface of a CuCat (0.5A-20s-Cu) was studied by quasi *in-situ* X-ray photoelectron spectroscopy (XPS) (Figure 5). Details about the XPS measurements and evaluation have been described elsewhere.[14b] The Auger spectra were fitted with the line shape of $Cu^{I}_2O$, $Cu^{II}O$, and metallic Cu reference spectra (Figure 5b). Without any further electrochemical treatment, the as-prepared CuCat contained 17% $Cu^0$, 66% $Cu^{I}_2O$, and 27% $Cu^{II}O$. After performing a cycling protocol, consisting of three CVs (Figure S10, 3) and a LSV (Figure S11), no more oxides can be detected at the surface. XPS after catalytic operation for 20 min shows that the CuCat surface remains metallic. Air exposure of the as deposited film seemingly causes a strong oxidation of the surface of the CuCat (mixture of 66% $Cu^{I}_2O$ and 27% $Cu^{II}O$).

In conclusions, the oxide species present in the as-deposited CuCat film are not stable at negative potentials, but they readily become reduced to metallic copper. A remaining minority fraction of sub-surface oxides that is below the detection limit of our experiments is not fully excluded. Complete reduction of the initially present Cu oxides likely occurs already at -0.2 $V_{RHE}$ (Figure S10). The transformation of the Cu oxides into metallic copper results in a disordered metallic phase, possibly with a metallic surface that offers a variety of non-crystalline arrangements of copper atoms.

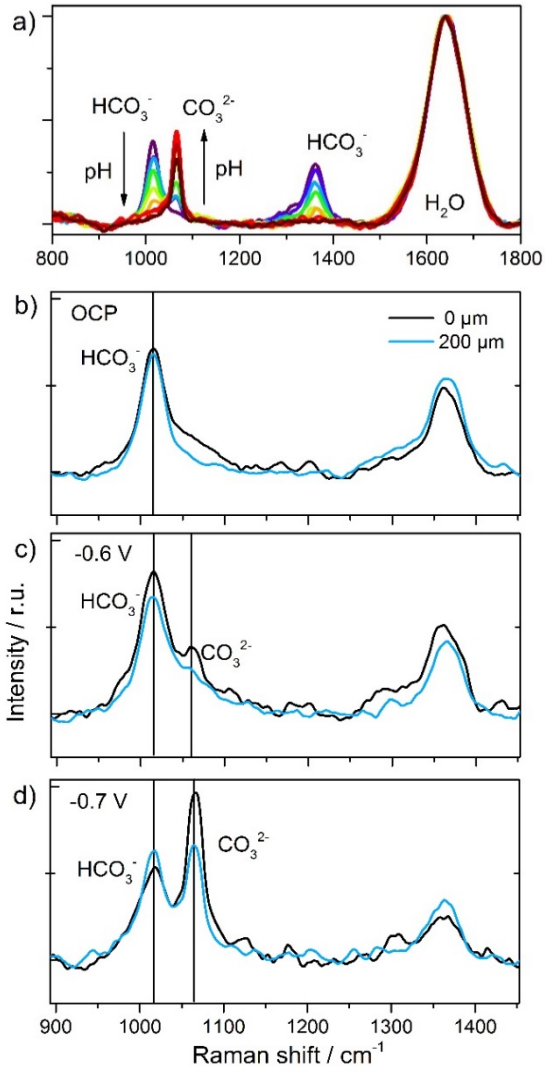


**Figure 6**. (a) Reference Raman spectra of 0.1 M $KHCO_3$ at different pH values (6.8, 8.8, 9.0, 9.5, 10.0, 10.5, 11.0, 11.5, 12.0, 12.5). The pH was adjusted by addition of KOH. (b-d) *Operando* Raman spectra of CuCat-0.5A-20s on Cu at OCP (b), at -0.6 $V_{RHE}$ (c), and at -0.7 $V_{RHE}$ (d) in 0.1 M $KHCO_3$ (bulk pH 6.8) directly at the surface (0µm – black line) and 200 µm far away from the surface (blue line).

**Evidence for pronounced local alkalization**

To demonstrate that CuCats experience diffusion-limited proton supply and thus local alkalization, we investigated the $HCO_3^-/CO_3^{2-}$ equilibrium via *operando* Raman spectroscopy. With increasing pH, the $HCO_3^-/CO_3^{2-}$ equilibrium generally shifts towards $CO_3^{2-}$, resulting in a decrease in the 1015 and 1363 $cm^{-1}$ Raman bands ($HCO_3^-$) and an increase in the 1065 $cm^{-1}$ band ($CO_3^{2-}$) (Figures 6a, S22-25). Figure 6 shows *operando* Raman spectra of a selected CuCat (0.5A-20s-Cu) at OCP and comparably low overpotentials (-0.6 and -0.7 $V_{RHE}$) in $CO_2$ saturated 0.1 M $KHCO_3$ buffer.

At OCP, mostly $HCO_3^-$ is detected at the CuCat surface, as expected (Figure S24). However, already at -0.6 $V_{RHE}$ directly at the surface a $CO_3^{2-}$ band is observed. At -0.7 $V_{RHE}$ the 1065 $cm^{-1}$ band is strongly enhanced compared to the 1015 $cm^{-1}$ band. Comparison to the reference spectra (Figure S24) shows that the local pH at -0.6 $V_{RHE}$ is 9.0 and drops to 7.8 at 200 µm distant from the electrode. At -0.7 $V_{RHE}$ the local pH is higher than 10 and alkalization is still detectable at a distance of 200 µm away from the surface, where the pH exceeds 9.5. Figure S25 shows that on Cu foil the local alkalization at low overpotentials is strongly reduced compared to the surface of Cu foam (at -0.6 $V_{RHE}$ around pH 7.8, at -0.7 $V_{RHE}$ smaller than 9.5).

We conclude that already at low overpotentials the CuCat is exposed to a drastic local pH increase, likely relating to diffusion limitations of $HCO_3^-$ ions which act as proton carriers (in analogy to the role of $H_2PO_4^-$ in water oxidation at neutral pH, see ref.[32]). The "local pH" is a macroscopic property because alkalization is detectable not only directly at the catalyst surface but also at a distance of 200 µm. We think that the relation (ratio) between proton-consuming catalytic processes and macroscopic proton movements is decisive for the extent of alkalization.

**Correlating ECSA with partial current densities**

The major detected products for $CO_2$ electroreduction on CuCats are CO, $CH_4$, $C_2H_4$, $HCOO^-$, and minor products are $C_2H_5OH$, and $C_3H_7OH$, $C_2H_6$, $C_3H_6O$ (Figures S26-30), with a stable product yield over the course of 8 h (Figure S31). When comparing $CO_2$-reduction product spectrum of the various electrodeposited Cu foams and a Cu foil, clear differences are observed. The formation of minor products is generally enhanced on Cu foams compared to Cu foil, but no distinct trends can be easily deduced for the minor products form the complex data shown in Figures S26-30. However, we observe interesting (and often surprising) quantitative relations between electrochemical surface area (ECSA) and partial current densities for $H_2$ (at -0.6 $V_{RHE}$), $CH_4$ (at -1.05 $V_{RHE}$), CO (at -0.6 $V_{RHE}$), and $C_2H_4$ (at -0.85 $V_{RHE}$). In the following, we focus on these informative relations, which are summarized in Figure 7 (and Figure S32 after normalization to ECSA).

*Methane formation is independent of internal surface area.* As opposed to the total current density and other partial current densities, $j_{CH4}$ is *not* enhanced by the increased ECSA of the CuCat foams (Figure 7b). This surprising behavior can be explained by a rate of $CH_4$ synthesis that is determined by the area of the macroscopic, outer surface of the catalyst material ($A_{out}$), but largely insensitive to the area of the nanoscopic inner surfaces of the CuCat foam ($A_{int}$). The outer, macroscopic surface areas correspond to the macroscopic electrode area covered by the CuCat foam. This area determines the macroscopic diffusion fluxes of educts and products from the bulk electrolyte to the catalyst foam and vice versa. (For formation of the pronounced crater structures with diameters exceeding 35 µm, as observed in the 1.0A-20s-Cu foam, the effective macroscopic surface area may be larger than for the electrode surface.)

The outer, macroscopic surface areas are approximately the same for Cu metal foils and all the porous Cu foams, whereas the inner surfaces are up to 65-fold larger in the herein investigated Cu foams (as judged by the ECSA determined in a non-catalytic potential range). It has been suggested that rougher surfaces suppress $CH_4$ formation due to a rise in the local pH, because $CH_4$ formation involves rate-determining, pH-dependent CO protonation steps.[2b, 11, 12b] Based on our Raman results indicating pronounced alkalization and in line with earlier reports[9a, 11, 33], we thus attribute a suppression of $CH_4$ production to locally reduced proton concentrations resulting from macroscopic diffusion limitations in the supply of protons to the CuCat electrode. Only for the CuCat with highest ECSA (65 cm²), $j_{CH4}$ is elevated compared to the pure Cu foil. This could relate to the characteristic dimensions of large enough surface structures that enhance the macroscopic outer surface, which is relevant for $CH_4$ formation.

**Figure 7**. Geometrical partial current densities of CuCats and Cu foil in

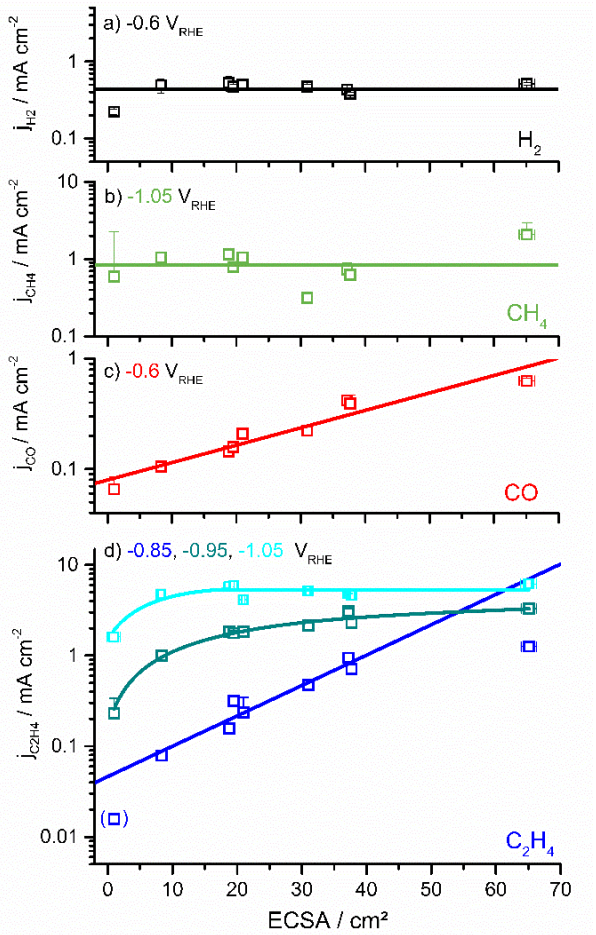


dependence of the electrochemically active surface area (in cm²). Partial current densities were determined at -0.60 $V_{RHE}$ for $H_2$ (black) (a), at -1.05 $V_{RHE}$ for $CH_4$ (green) (b), at -0.60 $V_{RHE}$ for CO (red) (c), and at -0.85 (blue), -0.95 (dark cyan), and at -1.05 $V_{RHE}$ (cyan) for $C_2H_4$ (d) in $CO_2$ saturated 0.1 M $KHCO_3$ (pH 6.8). ECSA was calculated from experimental double-layer capacitances, $C_{DL}$ (mF) (Figure S6, S7). Y-error bars correspond to the average of three individual measurements, and x-errors indicate the accuracy of determined ECSA. The data point in parenthesis is at the $C_2H_4$ detection limit; the real current density could be lower. Slope values of linear regressions are: (c) $j_{CO}$ 63.4±0.6 cm² $dec^{-1}$, and (d) $j_{C2H4}$ 35.7±0.2 cm² $dec^{-1}$.

*$H_2$-formation is independent of internal surface area.* Figure 7a shows that at -0.6 $V_{RHE}$, the $H_2$-evolution partial current stays at the same level for all CuCat foams, irrespective of their ECSA. This means that the $H_2$-evolution current densities per ECSA are strongly suppressed in a high-area foam when compared to low-area foams (Figure S32). The $CH_4$ and $H_2$ partial currents thus behave highly similar suggesting a similar mechanistic explanation: A pronounced local alkalization results from macroscopic diffusion limitations in the supply of protons to the CuCat electrode, which limits the $H_2$-formation current density and suppresses the relative yield of $H_2$-formation when compared to CO formation. An alternative explanation might be poisoning of inner CuCat surfaces by adsorbed *CO, which is discussed further below (and judged as being less likely).

*CO formation follows internal surface area.* In the CuCat foams, $j_{CO}$ increases pronouncedly with increasing ECSA (Figure 7c), in strong contrast to $j_{H2}$ (Figure 7a) and $j_{CH4}$ (Figure 7b). The regression line in Figure 7c corresponds to an exponential increase, but does not provide strong evidence for a truly

exponential behavior. An alternative presentation of the area-normalized partial current densities suggests that the $j_{CO}$ is directly proportional to ECSA (roughly constant value of $j_{CO}$/ECSA in Figure S32). A proportional increase of partial current density and ECSA may be viewed as being the "normal" behavior. Accordingly, the partial current densities of to $j_{H2}$ (Figure 7a) and $j_{CH4}$ (Figure 7b) do not behave normally. After normalization to ECSA, they are strongly suppressed at increasing ECSA (Figure S32). Again, diffusion limitations of protons may provide a possible explanation: Depletion of proton transporting carbonate ions results in pronounced alkalization[17b] at the active sites of CO formation within the CuCat foams which inhibits $CH_4$ formation generally and $H_2$ formation at least at low overpotentials, whereas CO formation proceeds via a largely pH insensitive pathway.[9a, 9d, 19, 35]

*Foam-enhanced $C_2H_4$ formation from two CO precursor species?* In the CuCat foams, $j_{C2H4}$ at -0.85 $V_{RHE}$ increases especially strongly with increasing ECSA (Figure 7d). Taking into account that such enhancement is not observed at higher overpotentials (-0.95, -1.05 $V_{RHE}$; cyan and blue lines in Fig. 7d), it corresponds to a lowering of the onset potential for $C_2H_4$ formation by increasing surface area in the foam interior. At -0.85 $V_{RHE}$, the $C_2H_4$ partial current of the pure metal foil is below the detection limit so that the cavities of the foam may be conceived as an essential prerequisite for low-potential $C_2H_4$ formation. Interestingly $j_{C2H4}$ (-0.85 $V_{RHE}$) increases clearly more strongly with increasing ECSA than $j_{CO}$ (-0.6 $V_{RHE}$). Whereas for $j_{CO}$ the partial current densities per ECSA are constant, the "normal" behavior, there is a strong increase in $j_{C2H4}$ per ECSA when comparing low-area with high-area foams (Figure S32). This behavior could result from a bimolecular reactions between (i) two adsorbed *CO species or (ii) between one adsorbed *CO and dissolved carbon species. We emphasize that the solid lines in Figure 7 represent a drastic approximation, but still may hint towards a quantitative trend. Their slope differs by a factor of about 2, which is in line with a quadratic dependence of $j_{C2H4}$ on the rate of CO production or number of adsorbed *CO molecules, thus supporting formation of one $C_2H_4$ molecule from two precursor species in a bimolecular reaction.

*Role of *CO coverage.* Interestingly, the CO partial current density is directly proportional to the magnitude of the irreversible redox wave likely assignable to formation of adsorbed *CO, as visible in Figure 8. (The CuCat with the highest ECSA represents an outlier, which again may be explainable by its large macropores increasing the effective outer surface versus the inner surfaces that dominate the ECSA.) This clear correlation can be straightforwardly explained as follows: The chemisorbed *CO equilibrates with gaseous CO in solution resulting in direct proportionality of *CO coverage and CO release. The redox-wave in the cyclic voltammogram becomes visible because largely complete *CO coverage of $CO_2$-reduction sites in the foam interior is reached already at about -0.7 $V_{RHE}$, resulting in a drop of the net partial current density for CO formation at more negative potentials. The outlined events also can explain that the rate of CO formation is not increasing significantly at higher overpotentials in most of the investigated copper foams. Comparison of the *CO reduction charge to the redox-active surface area indeed reveals that a major fraction of surface sites could be occupied by chemisorbed *CO molecules, as suggested by the following order-of-magnitude estimate for the surface area per absorbed CO molecule ($A_{*CO}$ for CuCat/1A-10s-Cu; *e*, elementary charge):

$$A_{*CO} = ECSA/(q_{red}/2e) \quad (3)$$
$$A_{*CO} = 37.7\ cm^2/(9.1\ mC/3.2 \cdot 10^{-19}\ C)$$
$$A_{*CO} = 13.2 \cdot 10^{-20}\ m^2 = 13.2\ Å^2 \approx 3.6\ Å \cdot 3.6\ Å$$

The above surface area per adsorbed *CO, which corresponds to about two copper surface atoms, likely is overestimated due to concomitant CO release, but it nonetheless demonstrates that a near-saturating level of *CO coverage is conceivable. Blockage of $H_2$ by *CO 'poisoning' within the copper foam might contribute to suppression of $H_2$ formation in the copper foam interior. However, our data suggest that the *CO coverage per ECSA is similar for low-area and high-area copper foams (but non-detectable for the metallic Cu foil). Therefore we consider it unlikely that *CO poisoning determines the activity trends shown in Figure 7.

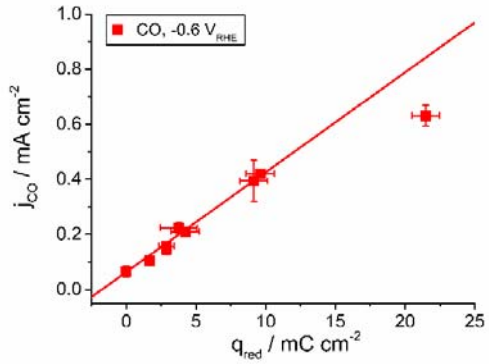


**Figure 8.** Geometric partial current density of CO in mA $cm^{-2}$ vs $q_{red}$ (or *CO adsorption charge) in mC $cm^{-2}$. The charge was obtained by integrating the plateau observed in the 2nd cycle of CVs (Figure 3) of CuCats. Linear regression (red line) excludes 1.0A-20s-Cu with ECSA of 65 $cm^2$. X- and y-error bars correspond to the average of three individual measurements.

A bimolecular reaction of CO species present in the foam cavities implies that for continuous catalytic operation, the effective residence time of chemisorbed *CO and gaseous CO is a crucial determinant of the rate of $C_2H_4$ formation. Aside from catalytic CO formation and conversion, the concentrations of chemisorbed *CO and gaseous CO molecules within the Cu foams are determined by the *CO/CO equilibrium within the cavities as well as diffusion of gaseous CO molecules from the inner-foam cavities to the bulk electrolyte. The resulting *CO/CO concentrations may also be discussed in terms of an effective *CO/CO residence time. This residence time is predicted to increase strongly with an increase in the foam-internal surface area in comparison to the outer, macroscopic surface. Enhanced $C_2H_4$ formation efficiency for small average distances between Cu nanoparticles has been explained by a similar line of arguments.[16]

## Conclusions

### Role of copper oxides

The electrodeposited Cu foams initially consist of both, Cu oxide (predominantly $Cu^+$, but also $Cu^{2+}$) and crystalline metallic domains. Application of catalytic potentials, which are sufficiently negative for $CO_2$ reduction, results in massive reduction of the Cu

oxides such that a metallic copper phase prevails at catalytic potentials. However, this metallic copper differs from polycrystalline copper metal by increased atomic disorder of the bulk material. We cannot exclude that this disordered metallic copper contains dispersed (sub-surface) oxygen atoms, but likely without formation of any distinct $Cu_2O$ or CuO domains, and not predominantly in form of a surface oxide. We note that all the investigated copper foams contain an initially high oxide content. Therefore, it is unlikely that the major reactivity trends observed within the series of copper foams are determined by the initially present oxide fraction, which is transformed into a disordered metallic phase at catalytic potentials.

**Rather than morphological details, $A_{in}/A_{out}$ determines product yields**

A hydrogen-bubble template method for Cu electrodeposition produced foams of 40-360 µm thickness. A variety of pore dimensions and morphologies were obtained, depending on deposition current, deposition time and choice of the metal employed as a substrate electrode during Cu electrodeposition (Pt versus Cu). For all these foams, only about 2% of their total volume is filled by metallic copper resulting in a total pore volume close to 98%. In spite of drastic morphology variations, the foam density remains approximately constant. In contrast, the ECSA, which measures the ratio between foam-internal surfaces ($A_{in}$) and the outer macroscopic surface ($A_{out}$), depends on the film morphology and is strongly enhanced for electrodeposition on a Cu substrate, explainable by a pronouncedly dendritic structure of the internal foam surfaces. The variability of the foam morphology promotes identification of properties that are determinants of catalyst specificity and achievable partial current densities. Eventually we find that it is neither the total internal pore volume nor specific morphological details, but it is the area of inner surfaces that is decisive regarding specificity and partial current densities at low overpotentials.

**Factors controlling specific partial current densities**

Formation of CO, and $C_2H_4$ at low overpotentials is strongly favored by large foam-internal surface areas, as opposed to $H_2$ and $CH_4$ formation. We propose that the detected correlations between partial current densities and $A_{in}/A_{out}$ are explainable within the following scenarios:

I. Macroscopic diffusion limits the proton supply and results in pronounced alkalization at CuCat surface, as shown herein by *operando* Raman spectroscopy. Because of low proton activity, $H_2$ and $CH_4$ formation are strongly suppressed, whereas CO and $C_2H_4$ formation still proceed via a largely pH-independent mechanism.[2b, 9a, 19, 35a].

II. Formation of chemisorbed *CO molecules could block active surface sites and thereby might suppress formation of $H_2$. [6c, 10d, 16-17, 37] We find that the fraction of surface sites covered by *CO could be significant. However, this fraction is not found to be significantly greater in high-area foams than in low-area foams. Consequently, we consider it unlikely that *CO poisoning of $H_2$-formation is a decisive determinant of the reactivity trends reported in our study.

III. Whereas $j_{CO}$ increases roughly in parallel to the ECSA of the CuCat foams, a clearly stronger increase is observed for $j_{C2H4}$. Taking into account also our finding that $j_{CO}$ may be directly proportional to the surface-adsorbed *CO molecules, we propose that $C_2H_4$ is formed within the foam from two CO precursor species, namely adsorbed *CO and dissolved CO present within the foam cavities.

## Experimental Section

**Synthesis:** Electrodeposition of Cu/$Cu_2O$-based catalysts (CuCats) follows a modified protocol described by Shin et al.[21a]. Three electrodes in a single compartment open electrolysis cell were used without stirring or heating. As reference electrode a Ag/AgCl electrode (Methrom), as counter electrode Pt foil were used, and the working electrode was cleaned and etched Cu or Pt foil (0.1 mm thickness, 99.99+% purity, Goodfellow) controlled by a Biologic SP300 potentiostat. Negative currents of 0.5 A or 1.0 A were applied for either 10 s or 20 s. The distance between the counter and working electrode was kept constant at ~3 mm. The electrolyte consisted of 0.2 M $CuSO_4$ and 1.5 M $H_2SO_4$. Before use the Cu or Pt foil was polished with diamond paste (0.7 µm), cleaned with ~10% $HNO_3$, and then cleaned stepwise in an ultrasonic bath using-milliQ $H_2O$ and ethanol. Immediately before electrodeposition the foils were etched with ~10% $HNO_3$ (in case of Cu) or with ~10% HCl (in case of Pt). The backside of the substrates was covered with silicon glue. Dark red films are obtained, which are washed with milliQ water, followed by dry blowing with $N_2$ gas. Unless otherwise stated prior to any further ex-situ analysis, the surface oxides have been reduced with a set of CVs (100 mV $s^{-1}$, from 0 to -1.05 $V_{RHE}$) and LSV (5 mV $s^{-1}$, from -0.3 to -1.1 $V_{RHE}$).

The Cu foil (0.1 mm thickness, 99.9999% purity, AlfaAeser) used as a reference was polished with micro-polish alumina suspension (0.05 micron) on micro cloth, then cleaned stepwise in an ultrasonic bath using-milliQ $H_2O$, ethanol, and milliQ $H_2O$ each for 10 min, followed by etching in 10% $HNO_3$ for 30 s.

**Electrochemical and chromatographic analysis of gaseous products:** The electrochemical $CO_2$ reduction was carried out in a custom made gas tight two compartment electrochemical cell (Figure S9) separated by a Nafion 211 membrane using a Gamry Reference 600 potentiostat. All the potentials measured were compensated for *iR* drop and represented with respect to reversible hydrogen electrode (RHE). Aqueous 0.1 M $KHCO_3$ solution was used as the electrolyte after saturating with $CO_2$ gas (99.995 vol.%, Air Liquide) for 10 min. During electrolysis, the electrolyte in the working electrode (WE) compartment was purged with $CO_2$ from the bottom of the cell at a flow rate of 20 ml $min^{-1}$ using a calibrated mass flow controller. Along with this the electrolyte at the WE compartment was stirred continuously to achieve maximum mass transport of $CO_2$ to the electrode surface. A leak free Ag/AgCl reference electrode was placed in front of the working electrode of 1 $cm^2$ area. A Pt coil (Biologic) was used as the counter electrode and $CO_2$ was purged to the counter electrode compartment. The gaseous products of $CO_2$ reduction reaction were identified and quantified using an online gas chromatograph (GC) (Shimadzu GC-2014) coupled with the two-compartment electrochemical cell. The product gases were analyzed after 20 min and 1 h of electrolysis at a specified potential. No yield differences were observed between 20 min or 1 h. During sampling, $CO_2$ flow along with the product gases in the loop were injected into GC by switching a 10-port valve. The GC is equipped with a thermal conductivity detector (TCD) for the detection of $H_2$ and other permanent gases. A methanizer in series with a flame ionization detector (FID) is used for detecting CO and hydrocarbons. Ar of grade 5 is used as the carrier gas.

**Analysis of liquid products:** Quantitative analysis of the liquid products is performed in two separate chromatographers (A and B). A) The offline gas chromatographer of type Shimadzu GC-2010-Plus with AOC 150i (autosampling) was used for detection and quantification of the volatile liquid products such as *acetaldehyde, propionaldehyde, ethanol, propanol,*

*allyl alcohol and acetone*. Microliter amounts of liquid sample are injected and converted to gas phase at elevated temperature in a quartz liner, following which a part of the expanded gas is injected into the He carrier gas and to the column of type SH-Stabilwax for separation. Aldehydes and alcohols were detected via a flame ionization detector (FID). Calibration was performed regularly for six above named products. B) HPLC of brand Agilent Technologies 1200 Series was used for separation, detection and quantification of the carboxylic acids such as formate and acetate. Separation is done in a Organi-Acid Resin column flushed with 0.005 M $H_2SO_4$ at 1 mL/min flow. Detection is achieved via refraction index detector (RID). Calibration was performed for formate and acetate.

**Electrochemically active surface area:** Electrochemical capacitance of the samples was determined using cyclic voltammetry[10a, 36] at 8 different scan rates (10, 20, 30, 40, 50, 60, 80, 100 mV/s). Non-Faradaic responses were found in potential ranges of 0.15 V around the open circuit potential (OCP). All currents in this region can be assigned to double-layer charging.[36c] Prior to each CV, the starting potential of the sample was held for 10 s. The charging current, *i*, (as average of absolute values of anodic and cathodic sweep) of the double layer is equal to the product of the scan rate, *v*, and the electrochemical double-layer capacitance, $C_{DL}$:

$$i = v \cdot C_{DL} \quad (4)$$

When plotting the averaged current, *i*, against the 8 different scan rates, *v*, the slope of the linear fit of the data equals the double layer capacitance, $C_{DL}$, of each sample. Calculation of the electrochemically active surface areas (ECSA) was done using eq 5. For $C_s$ we used an experimental double layer capacitance value of 38 ±3 µF for Cu foil.

$$ECSA = {}^{C_{DL}}/_{C_s} \quad (5)$$

**X-ray spectroscopy:** Cu *K*-edge XAS was performed at beamline KMC-3 at Helmholtz-Zentrum-Berlin (BESSY II) at 20 K. Energy calibration was done by collecting spectra of Cu metal foil (0.0075 mm, 99.99+ %, Goodfellow) and shifting the energy values according to the first inflection point of the first derivative of the Cu foil spectrum. Reference material spectra of CuO, CuCl, $CuSO_4$, $[Cu(OH_2)_6]^{2+}$ were collected in absorption mode with ionization chambers in front of and behind the sample. Spectra of Cu-based catalysts, Cu metal foil, and $Cu_2O$ were all collected in fluorescence mode with a 13 element windowless Germanium detector (Canberra) with detuned X-ray beam to avoid oversaturation and distortion due to the high metal content. The catalysts deposited on platinum were frozen in liquid $N_2$ after electrodeposition and performing three CVs and a LSV (0 to -1 $V_{RHE}$). In case of the copper substrate the thin catalyst films could not have been distinguished from the underlying substrate. Therefore, the catalyst layers have been carefully scratched off the surface using plastic razors. To guarantee that this method does not affect the atomic structure of the sample, we have compared the Cu *K*-edge spectra of a thin film on Pt and one scratched off the substrate surface. Figure S19 shows that no artefacts are introduced by this method and the atomic structure remains identical no matter if the sample is a thin film or a powder. Linear combinations of Cu and $Cu_2O$ were selected by least-square fits (with the weighting factors as fit parameters) which lead to identical results on XANES and EXAFS spectra.

*Operando* Cu *K*-edge measurements were performed at 293 K, largely as described previously.[37] The CuCat was deposited on carbon paper (FuelCellStore) for 0.5 A and 20 s. The deposited catalyst was placed in the window of a home-made electrochemical cell (Teflon) by connecting parts of pure carbon paper with Cu tape for electrode connection. The backside of the working electrode consisting of only carbon paper (facing the X-ray beam) was covered with Kapton tape. Close to the catalyst film (~ 0.2 mm), a small Ag/AgCl working electrode was mounted. A platinum coil was used as a counter electrode. The excited X-ray fluorescence passed through the Kapton window and then through a 10 µm Ni metal foil shielding against scattered light. The fluorescence was monitored perpendicular to the incident beam by a scintillation detector (19.6 $cm^2$ active area, 51BMI/2E1-YAP-Neg, Scionix; shielded by additional 2 µm Al foils against visible light). The detector consisted of a scintillating crystal (YAP) converting X-ray photons into visible light detected by a fast photomultiplier operated at 500 V connected to a Keithley multimeter for analog-to-digital data conversion. Absorption spectra of Cu metal foil were measured for precise energy calibration. In the beginning of each experiment, spectra of the dry film (as deposited) were collected. Then, 0.1 M $KHCO_3$, saturated with $CO_2$, pH 6.8 was filled into the cell, and during operation a constant $CO_2$ stream of 1 ml/min was kept in front of the film surface.

Details about the quasi in-situ XPS measurements and the corresponding data evaluation have been described elsewhere.[14b]

***Operando* Raman Spectroscopy**: Raman spectra were collected with a Renishaw inVia Raman spectrometer coupled with a Leica microscope. Calibration was done using a silicon wafer standard (521 $cm^{-1}$). A water immersion objective (Leica, 40×, numerical aperture = 0.8) was used to focus and collect the incident and scattered laser light during electrochemical measurements. A 0.013 mm thin optically transparent Teflon film (DuPont) was used to protect the objective from alkaline solution. The spectra were obtained in the range of 248 − 1869 $cm^{-1}$ using a grating with 2400 lines/mm and a slit size of 20 um. A 473 nm laser (YAG laser, 100 % power) focusing on a line (around 30 x 5 µm) served as an excitation source. The acquisition time for a spectrum with 5 accumulations was 35 s. A home-built spectro-electrochemical cell made of PTFE was interfaced with the Raman microscope for spectroscopic measurements. The cell was equipped with a Ag/AgCl reference electrode and a Platinum ring counter electrode, and controlled by a SP-200 Biologic potentiostat. To acquire spectra at different distances from the catalyst surface, we performed depth scans at each potential, employing the line-focus option of the inVia Raman spectrometer. The focusing point on void structure of our catalyst surface was set as 0 position. Before measurement, we performed three CVs and a LSV to reduce the surface oxides. The depth scans were performed in 0.1 M $KHCO_3$ electrolyte saturated with $CO_2$, and the electrolyte was continuously purged with $CO_2$ throughout the experiment. The desired potential was applied for 2 min before collecting the spectra to ensure steady-state conditions. All spectra were smoothed and baseline corrected by Renishaw software. Peak area analysis was carried out by in-house software “gloFit”.

Further experimental details can be found in the Supporting Information.

## Acknowledgements

This work was funded by the German Federal Ministry of Education and Research (Bundesministerium für Bildung und Forschung, BMBF) under grants 03SF0523B,A (CO2EKAT) as well as 033RCOO4D (eEthylene) and the European Research Council (OPERANDOCAT, ERC-725915), We thank the Helmholtz-Zentrum Berlin (HZB) for beamtime allocation at the KMC-3 synchrotron beamline of the BESSY synchrotron in Berlin-Adlershof and Dr. Ivo Zizak for special support. We thank Reza M. Mohammadi and Drs. Petko Chernev, Diego Gonzalez-Flores, Vadim Sikolenko, Stefan Mebs, and Michael Haumann for assisting in XAS data collection.

**Keywords:** $CO_2$ electroreduction • $Cu_2O$ • copper • surface area • Operando spectroscopy

## References


[1] a) M. Gattrell, N. Gupta, A. Co, *J. Electroanal. Chem.* **2006**, *594*, 1-19; b) D. D. Zhu, J. L. Liu, S. Z. Qiao, *Adv. Mater.* **2016**, *28*, 3423-3452; c) K. D. Yang, C. W. Lee, K. Jin, S. W. Im, K. T. Nam, *J. Phys. Chem. Lett.* **2017**, *8*, 538-545; d) J. P. Jones, G. K. S. Prakash, G. A. Olah, *Isr. J. Chem.* **2014**, *54*, 1451-1466.

[2] a) K. P. Kuhl, E. R. Cave, D. N. Abram, T. F. Jaramillo, *Energy Environ. Sci.* **2012**, *5*, 7050-7059; b) R. Kortlever, J. Shen, K. J. P. Schouten, F. Calle-Vallejo, M. T. M. Koper, *J. Phys. Chem. Lett.* **2015**, *6*, 4073-4082.

[3] a) J. W. Vickers, D. Alfonso, D. R. Kauffman, *Energy Technology* **2017**, *5*, 775-795; b) H. Mistry, A. S. Varela, S. Kühl, P. Strasser, B. R. Cuenya, *Nature Reviews Materials* **2016**, *1*, 16009.

[4] L. Zhang, Z.-J. Zhao, J. Gong, *Angew. Chem.* **2017**, *129*, 11482-11511.

[5] a) R. Reske, M. Duca, M. Oezaslan, K. J. P. Schouten, M. T. M. Koper, P. Strasser, *J. Phys. Chem. Lett.* **2013**, *4*, 2410-2413; b) K. Manthiram, B. J. Beberwyck, A. P. Alivisatos, *J. Am. Chem. Soc.* **2014**, *136*, 13319-13325.

[6] a) R. Reske, H. Mistry, F. Behafarid, B. Roldan Cuenya, P. Strasser, *J. Am. Chem. Soc.* **2014**, *136*, 6978-6986; b) H. Mistry, F. Behafarid, R. Reske, A. S. Varela, P. Strasser, B. Roldan Cuenya, *ACS Catalysis* **2016**, *6*, 1075-1080; c) Y. Huang, A. D. Handoko, P. Hirunsit, B. S. Yeo, *ACS Catalysis* **2017**, *7*, 1749-1756.

[7] a) B. Roldan Cuenya, *Acc. Chem. Res.* **2013**, *46*, 1682-1691; b) H. S. Jeon, S. Kunze, F. Scholten, B. Roldan Cuenya, *ACS Catalysis* **2018**, *8*, 531-535; c) D. Gao, I. Zegkinoglou, N. J. Divins, F. Scholten, I. Sinev, P. Grosse, B. Roldan Cuenya, *ACS Nano* **2017**.

[8] W. Luo, X. Nie, M. J. Janik, A. Asthagiri, *ACS Catalysis* **2016**, *6*, 219-229.

[9] a) A. S. Varela, M. Kroschel, T. Reier, P. Strasser, *Catal. Today* **2016**, *260*, 8-13; b) G. Z. Kyriacou, A. K. Anagnostopoulos, *J. Appl. Electrochem.* **1993**, *23*, 483-486; c) S. Kaneco, K. Iiba, K. Ohta, T. Mizuno, *J. Solid State Electrochem.* **1999**, *3*, 424-428; d) K. J. P. Schouten, E. Pérez Gallent, M. T. M. Koper, *J. Electroanal. Chem.* **2014**, *716*, 53-57; e) M. Akira, H. Yoshio, *Bull. Chem. Soc. Jpn.* **1991**, *64*, 123-127.

[10] a) X. Feng, K. Jiang, S. Fan, M. W. Kanan, *ACS Central Science* **2016**, *2*, 169-174; b) X. Feng, K. Jiang, S. Fan, M. W. Kanan, *J. Am. Chem. Soc.* **2015**, *137*, 4606-4609; c) C. W. Li, M. W. Kanan, *J. Am. Chem. Soc.* **2012**, *134*, 7231-7234; d) A. Verdaguer-Casadevall, C. W. Li, T. P. Johansson, S. B. Scott, J. T. McKeown, M. Kumar, I. E. L. Stephens, M. W. Kanan, I. Chorkendorff, *J. Am. Chem. Soc.* **2015**, *137*, 9808-9811.

[11] H. Mistry, A. S. Varela, C. S. Bonifacio, I. Zegkinoglou, I. Sinev, Y.-W. Choi, K. Kisslinger, E. A. Stach, J. C. Yang, P. Strasser, B. R. Cuenya, *Nat. Commun.* **2016**, *7*, 12123.

[12] a) T. T. H. Hoang, S. Ma, J. I. Gold, P. J. A. Kenis, A. A. Gewirth, *ACS Catalysis* **2017**, *7*, 3313-3321; b) S. Zhu, M. Shao, *J. Solid State Electrochem.* **2016**, *20*, 861-873; c) H. Xiao, W. A. Goddard, T. Cheng, Y. Liu, *Proc. Natl. Acad. Sci. USA* **2017**, *114*, 6685-6688.

[13] R. Kas, K. K. Hummadi, R. Kortlever, P. de Wit, A. Milbrat, M. W. J. Luiten-Olieman, N. E. Benes, M. T. M. Koper, G. Mul, *Nat. Commun.* **2016**, *7*, 10748.

[14] a) D. Kim, S. Lee, J. D. Ocon, B. Jeong, J. K. Lee, J. Lee, *Phys. Chem. Chem. Phys.* **2015**, *17*, 824-830; b) D. Gao, F. Scholten, B. Roldan Cuenya, *ACS Catalysis* **2017**, *7*, 5112-5120; c) C. S. Chen, A. D. Handoko, J. H. Wan, L. Ma, D. Ren, B. S. Yeo, *Catalysis Science & Technology* **2015**, *5*, 161-168.

[15] a) Y. Hori, A. Murata, R. Takahashi, *Journal of the Chemical Society, Faraday Transactions 1: Physical Chemistry in Condensed Phases* **1989**, *85*, 2309-2326; b) K. J. P. Schouten, Y. Kwon, C. J. M. van der Ham, Z. Qin, M. T. M. Koper, *Chem. Sci.* **2011**, *2*, 1902-1909; c) A. A. Peterson, F. Abild-Pedersen, F. Studt, J. Rossmeisl, J. K. Norskov, *Energy Environ. Sci.* **2010**, *3*, 1311-1315; d) F. Calle-Vallejo, M. T. M. Koper, *Angew. Chem. Int. Ed.* **2013**, *52*, 7282-7285; e) A. J. Garza, A. T. Bell, M. Head-Gordon, *ACS Catalysis* **2018**, *8*, 1490-1499.

[16] X. Wang, A. S. Varela, A. Bergmann, S. Kühl, P. Strasser, *ChemSusChem* **2017**, *10*, 4642-4649.

[17] a) H. Ooka, M. C. Figueiredo, M. T. M. Koper, *Langmuir* **2017**, *33*, 9307-9313; b) D. Raciti, M. Mao, C. Wang, *Nanotechnology* **2018**, *29*, 044001; c) C. Chen, B. Zhang, J. Zhong, Z. Cheng, *Journal of Materials Chemistry A* **2017**, *5*, 21955-21964.

[18] N. Gupta, M. Gattrell, B. MacDougall, *J. Appl. Electrochem.* **2006**, *36*, 161-172.

[19] M. Ma, K. Djanashvili, W. A. Smith, *Angew. Chem. Int. Ed.* **2016**, *55*, 6680-6684.

[20] S. Sen, D. Liu, G. T. R. Palmore, *ACS Catalysis* **2014**, *4*, 3091-3095.

[21] a) H. C. Shin, J. Dong, M. Liu, *Adv. Mater.* **2003**, *15*, 1610-1614; b) A. Dutta, M. Rahaman, N. C. Luedi, M. Mohos, P. Broekmann, *ACS Catalysis* **2016**, *6*, 3804-3814.

[22] a) T. N. Huan, P. Simon, G. Rousse, I. Genois, V. Artero, M. Fontecave, *Chem. Sci.* **2017**, *8*, 742-747; b) C. Reller, R. Krause, E. Volkova, B. Schmid, S. Neubauer, A. Rucki, M. Schuster, G. Schmid, *Advanced Energy Materials* **2017**, 1602114-n/a.

[23] Y. Lum, W. Ager Joel, *Angew. Chem. Int. Ed.* **2018**, *57*, 551-554.

[24] L. Mandal, K. R. Yang, M. R. Motapothula, D. Ren, P. Lobaccaro, A. Patra, M. Sherburne, V. S. Batista, B. S. Yeo, J. W. Ager, J. Martin, T. Venkatesan, *ACS Applied Materials & Interfaces* **2018**, *10*, 8574-8584.

[25] B. J. Plowman, L. A. Jones, S. K. Bhargava, *Chem. Commun.* **2015**, *51*, 4331-4346.

[26] Y. Hori, A. Murata, R. Takahashi, S. Suzuki, *J. Chem. Soc., Chem. Commun.* **1988**, 17-19.

[27] R. Kortlever, K. H. Tan, Y. Kwon, M. T. M. Koper, *J. Solid State Electrochem.* **2013**, *17*, 1843-1849.

[28] A. D. Handoko, C. W. Ong, Y. Huang, Z. G. Lee, L. Lin, G. B. Panetti, B. S. Yeo, *J. Phys. Chem. C* **2016**, *120*, 20058-20067.

[29] A. Wuttig, C. Liu, Q. Peng, M. Yaguchi, C. H. Hendon, K. Motobayashi, S. Ye, M. Osawa, Y. Surendranath, *ACS Central Science* **2016**, *2*, 522-528.

[30] M. D. Merrill, R. C. Dougherty, *J. Phys. Chem. C* **2008**, *112*, 3655-3666.

[31] D. G. Philipp Grosse, Fabian Scholten, Ilya Sinev, Hemma Mistry, Beatriz Roldán Cuenya *Angew. Chem. Int. Ed.* **2018**.

[32] K. Katharina, R. Franziska, Z. Ivelina, H. Jonathan, C. Petko, G. F. Diego, R. Marcel, F. Anna, D. Holger, *ChemSusChem* **2014**, *7*, 1301-1310.

[33] J. H. Montoya, C. Shi, K. Chan, J. K. Nørskov, *J. Phys. Chem. Lett.* **2015**, *6*, 2032-2037.

[34] H. Mistry, R. Reske, Z. Zeng, Z.-J. Zhao, J. Greeley, P. Strasser, B. R. Cuenya, *J. Am. Chem. Soc.* **2014**, *136*, 16473-16476.

[35] a) R. Kas, R. Kortlever, H. Yılmaz, M. T. M. Koper, G. Mul, *ChemElectroChem* **2015**, *2*, 354-358; b) K. J. P. Schouten, Z. Qin, E. Pérez Gallent, M. T. M. Koper, *J. Am. Chem. Soc.* **2012**, *134*, 9864-9867; c) F. S. Roberts, K. P. Kuhl, A. Nilsson, *Angew. Chem.* **2015**, *127*, 5268-5271.

[36] a) C. W. Li, J. Ciston, M. W. Kanan, *Nature* **2014**, *508*, 504-507; b) Y. Song, R. Peng, D. K. Hensley, P. V. Bonnesen, L. Liang, Z. Wu, H. M. Meyer, M. Chi, C. Ma, B. G. Sumpter, A. J. Rondinone, *ChemistrySelect* **2016**, *1*, 6055-6061; c) C. C. L. McCrory, S. Jung, J. C. Peters, T. F. Jaramillo, *J. Am. Chem. Soc.* **2013**, *135*, 16977-16987.

[37] D. Gonzalez-Flores, K. Klingan, P. Chernev, S. Loos, M. R. Mohammadi, C. Pasquini, P. Kubella, I. Zaharieva, R. D. L. Smith, H. Dau, *Sustainable Energy & Fuels* **2018**.